RESEARCH ARTICLE | MARCH 28 2007

Sound generation by a street of vortices in a nonuniform flow

Ting-hui Zheng; Georgios H. Vatistas; Alex Povitsky

Physics of Fluids 19, 037103 (2007)
https://doi.org/10.1063/1.2717177

Sound generation by a street of vortices in a nonuniform flow

Ting-hui Zheng[a)]
Department of Applied Mechanics, Sichuan University, 610065, People's Republic of China
Department of Building Service Engineering, The Hong Kong Polytechnic University, Hong Kong, People's Republic of China

Georgios H. Vatistas[b)]
Department of Mechanical and Industrial Engineering, Concordia University, Montreal, Quebec, Canada H3G 1M8

Alex Povitsky[c)]
Department of Mechanical Engineering, University of Akron, Akron, Ohio 44325-3903

(Received 6 June 2006; accepted 14 February 2007; published online 28 March 2007)

Propagation of acoustic waves originating from periodic vortices deforming in a nonuniform flow about a rigid body is examined numerically using a high-order compact finite-difference approximation. The governing equations are approximated by the linearized Euler equations in terms of disturbances. The aim of the study is to determine the sound directivity and strength as a result of the vortex street interaction with a solid body under subsonic base flow conditions. Both the vortex core diameter and vortex street spacing have a minor influence on the amplitude of the produced sound wave. When low-frequency vortex streets interact with a cylinder, the produced sound waves are very different from those that originated from high-frequency vortex streets. The interaction mechanism, sound generation, and propagation in a nonuniform flow are quite different for Taylor and Vatistas' vortex streets. In the case of a low-frequency Vatistas vortex street, the root-mean-square (RMS) value of the acoustic pressure has a well-defined sound directivity and amplitude. The former is greatly affected by the Mach number of the mean flow. For a high-frequency Vatistas vortex street, the RMS of acoustic pressure becomes highly nonmonotonic in the angular direction, while the mean flow Mach number has a moderate effect on the RMS angular profile. The striking differences in the sound amplitude and directivity for Taylor and Vatistas vortices are discussed in terms of their vorticity distribution. © *2007 American Institute of Physics*. [DOI: 10.1063/1.2717177]

I. INTRODUCTION

The interaction of a vortex with a solid body is important in the study of flow-induced vibration and sound generation. Furthermore, of fundamental significance is the case of a body following in the wake of another. Examples include (a) tip vortices shed by helicopter rotor blades moving downward that interact with the next blade, (b) rotor blades passing through the wakes of stator blades in turbomachinery, (c) vortex impingement on pipes that are in the wakes of upstream located tubes in heat exchanger tube banks, and (d) vortices shed by multielement airfoil where flaps are positioned in the wake of the main airfoil.[1]

This study was motivated by the airframe noise produced in aircrafts and the blade-vortex interaction (BVI) in helicopters. Previous studies of airframe noise identified high-lift devices and landing gears as dominant noise-producing components[2] during the landing phase of flight. While part of the landing gear noise is explained by wing and fuselage turbulent boundary layers, shedding vortices interacting with downstream-located rigid surfaces are also important sources of noise. Periodic vortices deforming in a nonuniform mean flow in the vicinity of a solid surface create repeated acoustic disturbances and produce sound that is often stronger than that created by turbulent eddies.[3,4] A good understanding of sound generation by these deforming vortices and the ability to predict accurately and reliably the generated sound is a necessary step toward reducing or controlling noise. The BVI noise is particularly bothersome since the last occurs usually near the ground as a rotorcraft slows and descends for landing. The frequency of this type of noise lies within the range of human sensitivity.[5] Thus, on one hand the BVI constitutes a source of environmental noise pollution in the commercial applications, and on the other hand it increases aircraft observability in military applications.

Although the topic of the BVI has been under scientific scrutiny for many years, especially for pointwise vortices and/or compact rigid bodies, much less is known about the noise generated by noncompact vortices. In this case, the size of the vortex and body are of the same order and neither of them is compact (small) relative to the acoustic wavelength.

Based on the orientation of the incident vortex with respect to the surface of the body, the vortex-body interaction can be categorized as[6] (a) a parallel or two-dimensional blade-vortex interaction where the axis of the vortex is perpendicular to the plane of the body, (b) a streamwise or per-

[a)]Electronic mail: tinghuizh@yahoo.com.cn
[b)]Electronic mail: vatistas@encs.concordia.ca
[c)]Electronic mail: povitsky@uakron.edu

pendicular vortex interaction where the axis of the vortex is aligned with the direction of the incident flow and perpendicular to the body surface, and (c) a normal vortex interaction where the axis of the vortex is perpendicular to the direction of the incident flow and orthogonal to the normal direction to the leading edge of the body. According to extensive experiments, the closer the BVI is to case (a), the greater the noise radiation. It is also known that a perpendicular vortex-blade interaction results in low levels of the produced noise.[7] In the current study, we concentrate on sound generated by a head-on two-dimensional parallel vortex impingement. In future research, the 3D effects of a nonparallel vortex and body axis, and the finiteness of the vortex tube, will be investigated.

In the considered BVI, eddies that are carried by the main flow may be distorted near the rigid surface and therefore radiate sound waves. Furthermore, the emanated waves, while propagating through the nonuniform high-speed flow, may be redirected, amplified, or weakened near rigid surfaces. While the downstream amplification of acoustic pressure and the accompanying shift in the wavelength are well documented in the literature, the upstream amplification of sound in flows around bodies immersed in the fluid has received less attention. The downstream amplification of sound occurs in both uniform and nonuniform flows, while the upstream amplification takes place only under the latter conditions. In a preliminary study by Povitsky,[8] the physical reasons for the upstream sound amplification in a nonuniform mean flow were studied for a flow about a nonlifting cylinder with the impulsive sound generation due to a single vortex. In the current study, we expand the previous work to account for the interactions of chains of vortices having different profiles of vortex velocity.

The physical space of sound generation can be schematically divided into three domains:[9] (i) the wake and boundary layer that is turbulent, highly viscous, and serves as a nursery of vortices; (ii) the low-turbulence nonuniform mean flow, in which viscous effects are minor; and (iii) the outer region with a uniform flow, in which the far-field noise prediction can be made by Lighthill's acoustic analogy, the Ffowcs-Williams–Hawkings equation, or the Kirchhoff integral.[10] When the radiated noise propagates in the flow, the mean velocity gradients are still significant. Therefore, integral methods that are often used to solve the far-field noise are not applicable to this domain, whereas the Euler equations may account for the sound propagation in a nonhomogeneous flow.

The profile of the flow in a vortex depends on the geometry of the upstream rigid body and the time interval between the vortex generation and its impingement on the downstream surface. The Vatistas vortex formulation was found to agree well with experimental data of a helicopter's tip vortices[11] when $n=2$ [formulas (3)] is considered. This model exhibits the key features of a viscous vortex. When the radius r approaches infinity, it behaves like a free vortex, which is also known as an irrotational vortex. As r tends to infinity, the vortex circulation approaches a constant nonzero value and the Vatistas vortex is a nonzero circulation vortex. When r approaches zero, it approaches a forced vortex, in which the fluid rotates as if it were a solid body. This vortex model appears to be very versatile; in other words, given different values of the parameter n, other self-similar vortex models can be obtained.[12]

The vortices created by localized stirring for a short period of time are known to follow Taylor's model with an exponentially decaying velocity profile. This type of whirl is routinely used in aeroacoustic research; see Inoue,[10] Colonius,[13] Visbal and Gaitonde,[14] and Povitsky.[8] When r approaches infinity, the vortex circulation tends to zero, and as such, Taylor's formulation is known as a zero-circulation vortex.

A recent study[15] investigated numerically how a single vortex being deformed in a nonuniform flow about a cylinder generates sound. On one hand, a comparison of profiles of several nonzero circulation vortices shows a similar acoustic wave pattern shown in another recent study,[16] with the Vatistas vortex profile using $n=2$ as the representative. On the other hand, distinctly different sound manifestations were obtained using the zero-circulation Taylor vortex. The goal of the current study is to determine what differentiates the sound radiated by Taylor's street from that radiated by that of Vatistas, and how the sound directivity and strength profile can be affected by the vortex street frequency, the strength, and the size of the vortex. Parametric studies conducted with the use of numerical simulations were aimed toward the understanding of the effects of the frequency of the vortex appearance in the street, the spacing between vortices, the vortex core size and its strength, and the mean flow Mach number on sound amplitude and directivity.

To solve the governing unsteady Euler equations, a linear expansion in terms of flow disturbances is used. In general, the coefficients in the obtained linearized system correspond to the compressible mean flow. In the current study, the coefficients are replaced with their incompressible approximation. The validity of such an approximation is discussed in Sec. II.

This approach replaces the direct simulation method of the unsteady flow by a flow decomposition into mean and perturbation problems. This approach does not allow the acoustic perturbation to backscatter into the flow solution. In this respect, the approach is similar to that of Hardin and Pope.[17] In the near field, the perturbation quantities are the differences between the unsteady compressible and steady flow-field variables. The perturbation quantities are equivalent to acoustic quantities in the far field. The variable split approach moderates the difficulties associated with resolving a small amplitude of acoustic wave fluctuations relative to the mean flow quantities, a long propagation distance of acoustic waves to the far field, and large acoustic temporal scales, characteristic for periodic vortices. As such, the approach provides an effective method of predicting acoustic fields resulting from a low-Mach-number, noncompact source region.[18]

The paper is arranged as follows. In Sec. II, the developed mathematical model and the numerical methods employed are described. In Sec. III, the nonreflecting boundary conditions and the code validation are presented. In Sec. IV, the sound generated by a two-row vortex street of alternating

sign is considered. The frequency effect, the vortex street spacing effect, and the vortex core size effect are also investigated.

II. MATHEMATICAL MODEL

In the adopted approach, the compressible unsteady flow field is represented as a sum of a steady flow field and an inviscid, acoustic perturbation field. The acoustic perturbation equations are obtained by subtracting the steady mean flow mass and momentum equations from the expanded unsteady Euler equations. The Euler equations are linearized about the given steady solution of the background flow.

The flow separation of the laminar boundary layer occurs slightly upstream of the equatorial section of the cylinder, whereas for the turbulent boundary layer the flow separation occurs downstream of the equatorial section. Therefore, the inviscid flow model can adequately describe the flow about the front part of the cylinder. For $M>0.41$, a shock wave is formed at the cylinder surface and the approach is no longer valid.

In general, the mean flow can be obtained analytically or numerically using regular numerical schemes with a low order of accuracy. The flow about a cylinder with $M_\infty<0.41$ is taken as a simple representative setup for noise propagation studies in a nonuniform subsonic flow. The use of true compressible flow, for which an analytical solution is not available, calls for a numerical solution of the mean flow equations that introduce numerical errors to coefficients. To describe the compressible mean flow about the cylinder, the $O(M^2)$ correction of the potential flow is introduced in Appendix A. Note that the analytical expression for the compressible correction to the velocity potential is available only for the circular cylinder.

The $O(M_\infty^2)$ components of acoustic equations (see Appendix A) represent an upper estimate of the error introduced by the replacement of the compressible mean flow with its incompressible approximation because of the following reasons: (i) the compressible correction φ_1 in (A4) approaches zero with the distance from the cylinder and (ii) the term $(M^2-M_\infty^2)$ in (A10) is smaller by the absolute value than M_∞^2 everywhere except for the vicinity of the stagnation point. Using a comparison of numerical solutions, Povitsky[8] demonstrated that the account for compressibility in the mean flow (i.e., the presence of the compressible correction to the flow and a variable density and the speed of sound) for $M_\infty<0.41$ leads to modest changes in the directivity of sound. In particular (see Fig. 14 in Ref. 8), this correction to the flow about the cylinder leads to an increase in the RMS of acoustic pressure by only 3% for $M_\infty=0.4$ and can be neglected for $M_\infty\leqslant 0.2$. The value of $M_\infty=0.2$ is a typical representative value for air vehicles in the landing phase of the flight where most of the airframe noise is produced.[19]

In the current study, approximate linearization is assumed by omitting components of the order of $O(M_\infty^2)$ and higher-order terms in (A10). The influence of the Mach number ranged from 0 to 0.4, as shown in Fig. 11, while the value of the Mach number equal to 0.2 is used for other current numerical experiments.

The background potential mean flow around the circular cylinder in polar coordinates is given by

$$U = U_\infty \cos\theta(1 - R_{\mathrm{cyl}}^2/r^2),$$

$$V = -U_\infty \sin\theta(1 + R_{\mathrm{cyl}}^2/r^2), \tag{1}$$

where U_∞ is the infinite flow velocity, R_{cyl} is the cylinder radius, and U,V are the mean flow radial and azimuth velocity components, respectively.

The nondimensional linearized approximate inviscid perturbation equations (A11) in polar coordinates are

$$\frac{\partial\rho'}{\partial t} = -\left(\frac{\partial u'}{\partial r} + \frac{u'}{r} + \frac{1}{r}\frac{\partial v'}{\partial\theta}\right) - U\frac{\partial\rho'}{\partial r} - \frac{1}{r}V\frac{\partial\rho'}{\partial\theta},$$

$$\frac{\partial u'}{\partial t} = -\frac{\partial p'}{\partial r} - U\frac{\partial u'}{\partial r} - \frac{\partial U}{\partial r}u' - \frac{1}{r}\left(V\frac{\partial u'}{\partial\theta} + \frac{\partial U}{\partial\theta}v' - 2Vv'\right) - \left(U\frac{\partial U}{\partial r} + \frac{1}{r}V\frac{\partial U}{\partial\theta} - \frac{1}{r}V^2\right)\rho',$$

$$\frac{\partial v'}{\partial t} = -\frac{1}{r}\frac{\partial p'}{\partial r} - U\frac{\partial v'}{\partial r} - \frac{\partial V}{\partial r}u' - \frac{1}{r}\left(V\frac{\partial v'}{\partial\theta} + \frac{\partial V}{\partial\theta}v' + Uv' + Vu'\right) - \left(U\frac{\partial V}{\partial r} + \frac{1}{r}V\frac{\partial V}{\partial\theta} + \frac{1}{r}UV\right)\rho', \tag{2}$$

where $\rho', u\prime, v'$ represent disturbance variables and U,V correspond to the U_0, V_0 in Appendix A.

In this study, the fourth-order-accurate central-difference compact scheme[20] and the explicit fourth-order Runge-Kutta time advancement[21] are chosen for the numerical approximation of the linearized Euler equations. In the reminder portion of the paper, primes indicating the disturbance variables are omitted for brevity. As mentioned earlier, the vortex models of Taylor[22] and Vatistas[12] are considered to compare generated acoustic waves.

The velocity distribution of Vatistas' vortex is given as follows:

$$v'_\theta = \frac{\Gamma}{2\pi} \times \frac{r}{\sqrt{R_c^{2n} + r^{2n}}}, \tag{3}$$

where v'_θ is the vortex tangential velocity, Γ is the maximum circulation as a function of r, r is the distance to the vortex center, and R_c is the size of the vortex core, which corresponds to the radius where the tangential velocity reaches its maximum; n is the parameter of the vortex profile.

For the Taylor vortex, the tangential velocity distribution is

$$v'_\theta = \frac{\Gamma}{2\pi}\frac{r}{R_c}\exp[1 - (r/Rc)^2]/2, \tag{4}$$

Figure 1 presents the profiles of the tangential velocity and the vorticity distribution with respect to the distance to the vortex center of Taylor's and Vatistas' vortices. It is then clear that the former vortex is highly localized in space (and for this reason is often used to represent concentrated vortices) while the latter vortex is very close to the Lamb-Oseen vortex characterized by a low-decreasing rate of the velocity

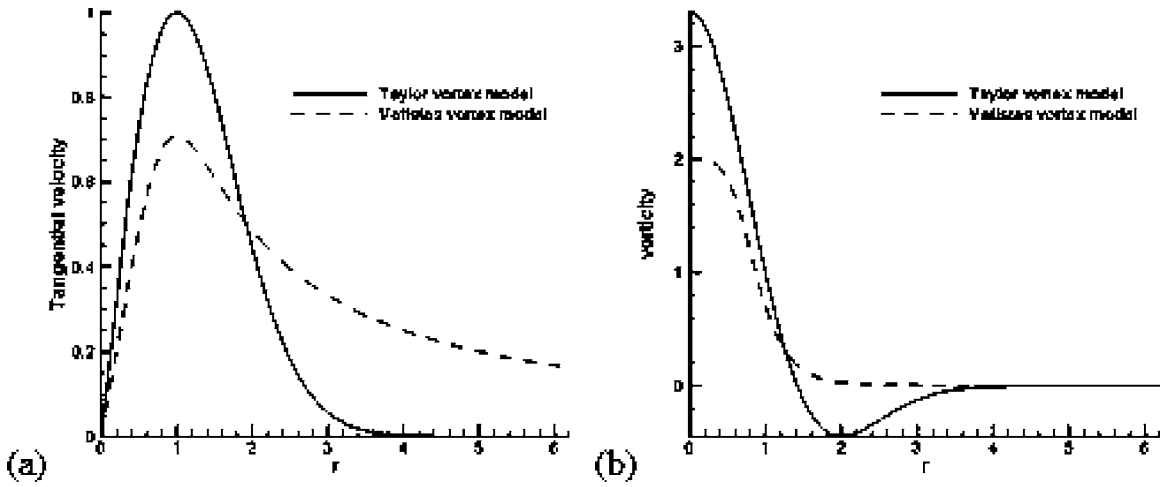

FIG. 1. Profiles of vortex tangential velocity (a) and vorticity (b) as a function of the distance to the vortex center.

field. Note that the vortex velocity profiles in Fig. 1 are presented in a normalized form with the maximum tangential velocity value of Taylor's vortex being equal to unity. In Fig. 1, the maximum circulation Γ for both Taylor's and Vatistas' vortices is the same. In terms of the total circulation of the vortex $\Gamma_T = \int \Omega dA$ (where Ω is the vorticity in the 2D flow and the integration area is too large to cover the entire vortex), the Taylor vortex is a zero-circulation vortex model, whereas the Vatistas vortex is a nonzero-circulation vortex model. Note that the maximum vorticity at the vortex center is ~50% larger for Taylor's vortex compared to Vatistas' [see Fig. 1(b)]. The vorticity profile for Vatistas' vortex is monotonic, whereas for Taylor's vortex the vorticity has negative area with its minimum located at $\sim 2Rc$.

Figure 2 shows an overview of the vortex street-cylinder framework.

The vortices are periodically superimposed on the flow (see Appendix B) with the constant time period, T, at the axial location $(-1, \pm D)$, i.e., at a distance of one radius upstream of the cylinder surface, where the local mean velocity $U = 0.75 U_\infty$. The vortex velocity components are added to the disturbance variables while the pressure field rapidly adjusts to the updated flow field. It has been verified in prior studies by the authors that this procedure does not generate sound waves.[8,15]

It has been shown[8] that the influence of the initial location of a vortex on the generated sound is small if the initial distance between the added vortex and the cylinder wall exceeds one cylinder radius. The Taylor vortex velocity, which is equal to 0.0002, is very small compared to the normalized background mean flow velocity ($M_\infty = 0.2$) and therefore it is possible to take the disturbance velocity as the sum of the computed disturbance generated by the existing vortices and the velocity introduced by the new vortex superimposed into the mean flow. Note that convection of vortices, their deformation, and the generation and propagation of sound are described in terms of unsteady components (disturbances) by the same linearized equations (2). Although the acoustic components and the strength of the vortices are of a different order of magnitude, both are much smaller than the mean flow field. The added vortices are, therefore, part of the disturbance flow field and not part of the mean flow.

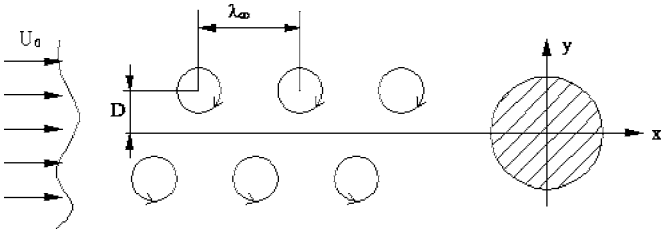

FIG. 2. Scheme of vortex street interaction with the cylinder.

The vortices are convected with the mean flow, so the wavelength λ_∞ of the undisturbed vortex street is given by $\lambda_\infty = 2TU$, where U represents the local stream velocity at the point where vortices were added. According to Gursul and Rockwell,[1] the vortex street-cylinder interactions can be classified based on the length scale λ_∞ of the vortex street. In this study, the sound generated by the vortex street-cylinder interaction was categorized based on the vortex street frequency $1/T$ into two groups. One typical frequency of vortex adding, $f = 1/0.5 = 2$, represents the low-frequency vortex street; the other typical frequency corresponds to $f = 1/0.05 = 20$ and represents the high-frequency vortex street. In the former case, $\lambda_\infty = 2^*0.5^*0.2^*0.75 = 0.15$ is bigger than the vortex core diameter ($2R_c = 0.08$), while in the latter case λ_∞ is substantially smaller than the vortex core diameter. Therefore, for a low-frequency case the core parts of the chain vortices do not interact before they approach the cylinder.

The root-mean-square of acoustic pressure (RMS) is obtained as a postprocessing of the disturbance pressure. In this investigation, the nonzero averaged acoustic pressure was observed. Humans respond to fluctuations of acoustic pressure (which may be referred to as "clean" RMS of acoustic pressure) as opposed to the elevated averaged value of RMS acoustic pressure. To obtain the clean RMS of acoustic pressure, P_{acous}, the averaged acoustic pressure P_{ave} is subtracted from the local RMS acoustic pressure P_{RMS},

$$P_{\text{acous}} = \sqrt{P_{\text{RMS}}^2 - P_{\text{ave}}^2}. \tag{5}$$

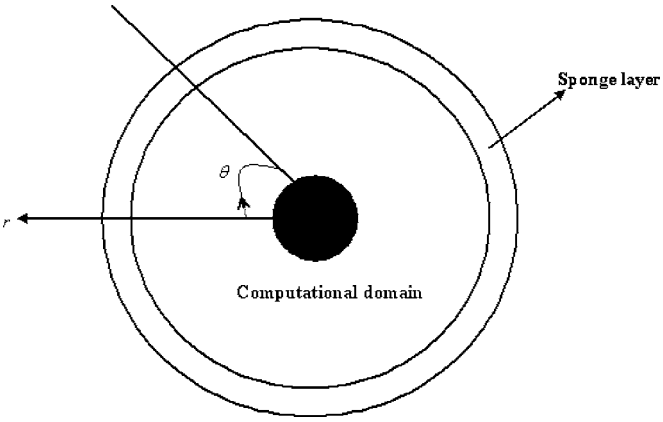

FIG. 3. Scheme of computational domain.

In the current study, the time-averaged RMS of acoustic pressure is presented relative to the time-averaged pressure rather than with respect to the basic state of pressure.

III. BOUNDARY CONDITIONS AND CODE VALIDATION

The computational domain is presented in Fig. 3.

When the vortex field is implemented as an initial condition for disturbance velocity, it may violate the nonpenetrating boundary condition if its core reaches the rigid wall. To satisfy the zero normal velocity boundary condition at the cylinder wall, a vortex image system,[23] in which the equal and oppositely spinning vortex of the same type was put at the inverse point inside the cylinder, and an equal vortex, were placed at the origin to satisfy the nonpenetrating boundary condition. The vortex image system was switched on only during the time intervals when the vortices were added, otherwise it was switched off (see Appendix B). The Taylor vortex is not affected by the image vortices because of its localized velocity distribution. In other words, the image of Taylor's vortices remains inside the cylinder and does not affect the flow field. On the contrary, the Vatistas vortex image system produces a correction to the original Vatistas formulation in infinite space. This approach was tested in the prior research of the authors.[15] The nonpenetrating boundary condition is satisfied by $dp/dn=0$ for the pressure disturbance; whereas the normal to the rigid surface component of the velocity is set equal to zero, and the tangential component of the disturbance velocity is extrapolated from the interior grid points using one-sided finite differences.[8,15] Vibration of the cylinder is neglected in this study. At the outer boundary, a sponge layer, which is a nonphysical domain, is set up[24] (see Fig. 3) and a damping term is added to the original governing equations,

$$\frac{\partial \vec{u}}{\partial t} + A\frac{\partial \vec{u}}{\partial x} + B\frac{\partial \vec{u}}{\partial y} + \sigma \vec{u} = 0, \tag{6}$$

where σ is the damping coefficient.

The purpose of the damping term is to eliminate the reflections of acoustic energy back into the computational domain. The background mean flow is switched off in the sponge layer. The damping term is given as follows:

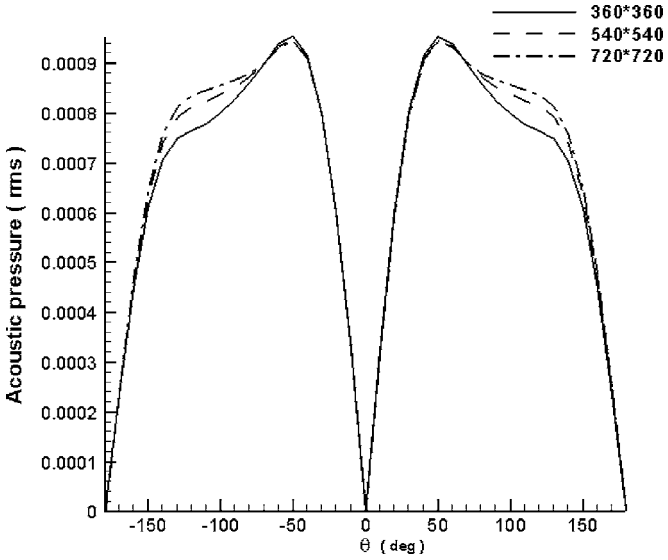

FIG. 4. The angular distribution of RMS of acoustic pressure for Vatistas' one-cell vortex with $n=2$.

$$\sigma_r = \sigma_m \left| \frac{r - r_{\text{out}}}{D_s} \right|^{\beta}, \tag{7}$$

where r_{out} is the outer boundary of the physical domain that coincides with the inner boundary of the sponge layer and D_s is the width of the sponge layer. The width of the sponge layer corresponds to 30 grid intervals in the current study. To compute σ across the sponge layer, the value of $\sigma_m=2/\Delta r$, where Δr is the grid step in the r direction and $\beta=2$.

The code used in the current study is based on the previously developed code for modeling of the single vortex interaction with solid surfaces.[8] It has been validated against known benchmark cases. For longer time integration, the benchmark case of the periodic acoustic source has been implemented and compared with available benchmark solution.[25]

A grid refinement study was conducted using a single Vatistas vortex interacting with a solid cylinder. The computational domain $\Omega=[0.5<r<3.0]\times[-\pi<\theta<\pi]$ is covered with 360×360, 540×540, and 720×720 uniform numerical grids. The RMS of acoustic pressure radiated by a single vortex interaction with the cylinder is shown in Fig. 4 with respect to the angle θ from the centerline. It was ascertained that the RMS of acoustic pressure profiles for 540×540 and 720×720 numerical grids was almost the same (the maximum difference was within 1%). Therefore, the 540×540 uniform numerical grid was used in the computations. The time step is computed by $\Delta t=C\Delta r$, where the Courant number, C, is taken equal to 0.1, 0.25, and 0.5, respectively. It was observed that the RMS of acoustic pressure profiles for the Courant numbers equal to 0.1 and 0.25 agree well with each other. In the following simulations, the Courant number equal to 0.25 is adopted.

IV. COMPUTATIONAL RESULTS

The free-stream velocity, U_∞, if not specified otherwise, was kept equal to 0.2, i.e., the Mach number in the far field

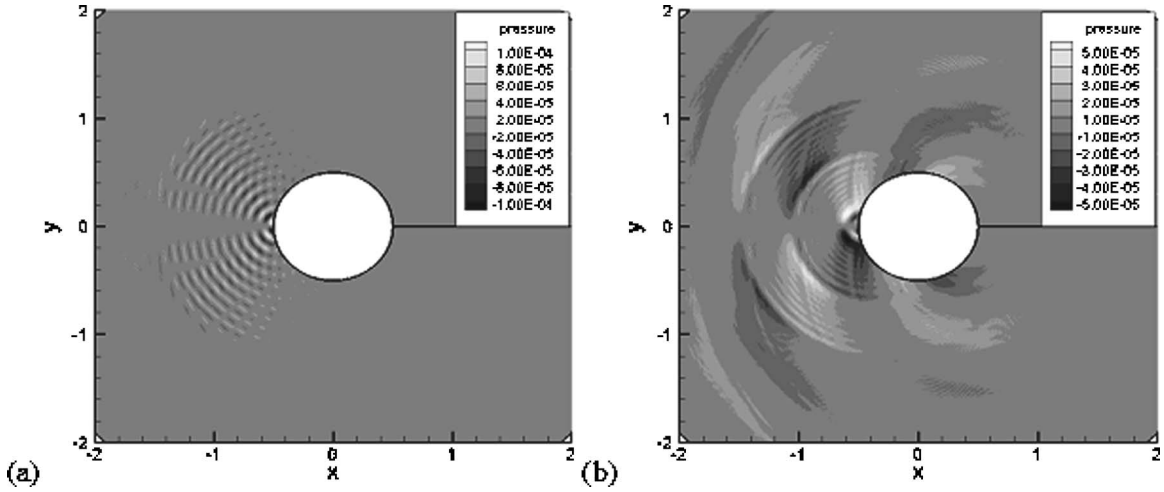

FIG. 5. Acoustic pressure isolines generated by Vatistas' vortex street at $t=10.0$: (a) high frequency, $f=1/0.05=20$, (b) low frequency, $f=1/0.5=2$.

was equal to 0.2. Taylor and Vatistas vortices have a vortex core radius $R_c=0.04$ and a circulation of 0.00005. Recall that the maximum tangential velocity for the Taylor vortex is equal to 0.0002 (see Sec. II).

First, the sound generation by the impingement of a single street of small vortices of an alternating sign was investigated. This is the limiting case of a two-row vortex street when the spacing between rows tends to zero. When the vortex is convected by the flow near the rigid surface of the cylinder, the vortex is strongly deformed by the nonuniform stagnation flow. The embedded vortices are distorted in the streamwise direction in such a way that their shape becomes elliptical. As a result of deformation of vortices, the pressure field becomes noncircular, producing pressure spots of alternating sign. As the deformation of the vortex and the pressure field continues, these spots elongate and generate pressure waves. This effect was discussed for a single vortex interaction with a cylinder.[15]

In Fig. 5, the acoustic pressure isolines, generated by the vortex street with the Vatistas vortex velocity profile at frequencies 1/0.05 and 1/0.5, are presented at time moments $t=10.0$. Silence zones near the centerline were observed for all cases as a result of the cancellation of sound waves for this symmetrical setup. Although there are ten times more vortices per time unit involved in sound generation by a high-frequency vortex street compared to the vortex street at a frequency of 1/0.5, the amplitude of sound waves radiated by these two vortex streets does not show such a large difference. For the Vatistas vortex street, the pressure amplitude corresponding to the high-frequency street is only about two times larger than the one corresponding to the low-frequency street. For the high-frequency Taylor vortex street, the pressure amplitude is only one and a half times larger than that for the low-frequency vortex street.

The RMS of acoustic pressure generated by a single vortex and by vortex streets are shown in Fig. 6 for comparison.

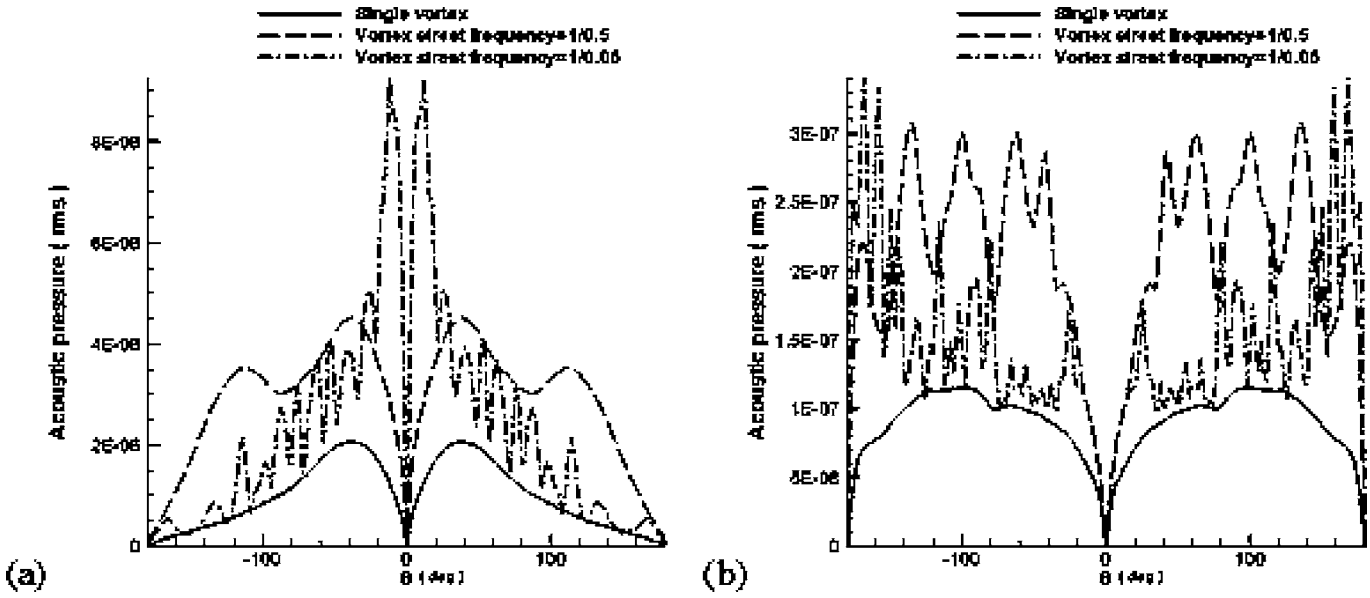

FIG. 6. The RMS of acoustic pressure distribution for a single vortex and for a one-row vortex street: (a) Vatistas' vortex and (b) Taylor's vortex.

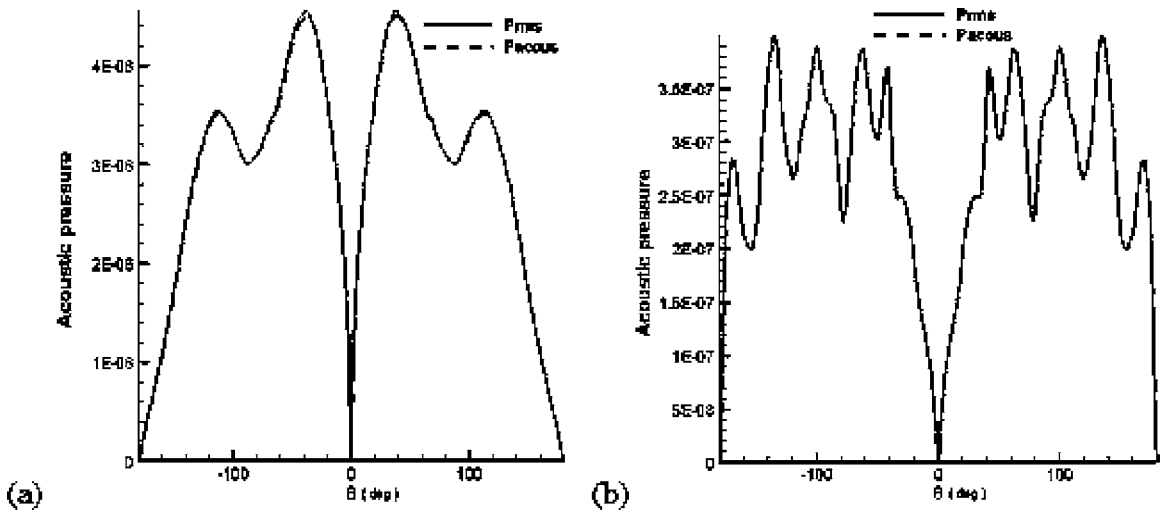

FIG. 7. Comparison of the RMS of acoustic pressure and RMS of disturbance pressure at frequency $f=2$: (a) Vatistas' vortex street, (b) Taylor's vortex street.

For Vatistas' vortex, the sound level increases with the street frequency and the sound directivity moves closer to the centerline. For a single vortex, the sound directivity has only one pair of local maxima whereas the number of maxima increases with the frequency of the adding of vortices. For instance, only two pairs of maxima are observed for the low-frequency chain ($f=2$). The acoustic pressure profile generated by the low-frequency vortex street ($f=2$) appears to be quite different from that generated by the high-frequency vortex street ($f=20$). For the low-frequency Vatistas vortex street, the RMS of acoustic pressure has two clear maxima, and the sound directivity makes an angle of 45° to the centerline. For the high-frequency Vatistas vortex street, the sound profile becomes strongly nonmonotonic with the angle θ, although there is still an obvious maximum amplitude at about 10° with the centerline. For the Taylor vortex street of any frequency, the sound directivity is highly nonmonotonic. For the low-frequency Taylor vortices street [see Fig. 6(b)], the sound profile appears to be nonmonotonic and it has a silence zone near the centerline. Note that for a single vortex, the RMS is five times larger for the Vatistas vortex than that for the Taylor vortex. The RMS for chains of Vatistas' vortices appears to be more than one order of magnitude larger than that for Taylor's vortices.

The angular distribution of the RMS of acoustic pressure, P_{RMS}, and the corrected RMS, P_{acous} [see Eq. (5)], are presented as a function of angle θ from the centerline in Fig. 7. It was observed in this case that the value of P_{RMS} is very close to P_{acous}; that is, the average pressure buildup is negligible. The modest asymmetry of sound profile with respect to the centerline was observed because of the time delay of the opposite-spinning vortex couples for both vortex streets.

The generated sound wave and its directivity are closely related to the deformation of vortices and their angular position with respect to the cylinder. The level of RMS of acoustic pressure is orders of magnitude larger for Vatistas' than for Taylor's vortices, and the sound that originated from the impingement of Taylor's is highly nonmonotonic with respect to angle θ (see Figs 6 and 7). Although the sound-reflecting body is noncompact here, integral formulas for acoustic pressure obtained for compact bodies can be considered for qualitative analysis (see Ref. 26, pp. 128–130 and 186–188). The magnitude of acoustic pressure is proportional to the $\int \vec{\omega} * \vec{v}$. In the considered 2D cases, the vorticity vector is one-dimensional. For the Vatistas vortex, the sign of vorticity remains the same, whereas for the Taylor vortex the sign alternates [see Fig. 1(b)]. The area of nonzero vorticity is approximately the same for both vortices [see Fig. 1(b)]. The reduced RMS for Taylor's vortices and the highly nonmonotonic directivity of RMS can be explained by the interference and mutual cancellation of positive and negative vorticities in the integral for acoustic pressure.

The effect of spacing between vortex streets D on sound generation and propagation was investigated for D equal to 0, 0.05, 0.1, 0.15, and 0.3. For these D, the values of RMS of P_{acous} are presented as a function of the angle θ in Fig. 8. For the Vatistas vortex street, as the spacing between the rows of vortices increases, the asymmetry appears to be more noticeable. The sound pressure on the lower half of the cylinder is somewhat larger than the sound pressure on the upper half of the cylinder, whereas the maximum amplitude of acoustic RMS increases slightly with the spacing between rows of vortices. Nevertheless, the sound wave profiles look alike for all different distances at the same vortex street frequency. That is, the sound directivity is almost invariant with the vortex street spacing. For the low-frequency Taylor vortex street, it appears that when the vortex street spacing is nonzero, a silence zone near the centerline disappears [Fig. 8(c)]. The change of the vortex street spacing does not significantly affect the sound amplitude; however, the sound directivity is fluctuating with D [see Fig. 8(d)]. Therefore, the vortex row spacing is one of the key coefficients for the cylinder-Taylor vortex interaction mechanism and sound pressure generation and propagation.

At time moment $t=10.0$, vortices were found downstream of the stagnation point. This indicates that after impingement of the chain of vortices on the cylinder, the vortices do not disappear, but rather they move down the stream

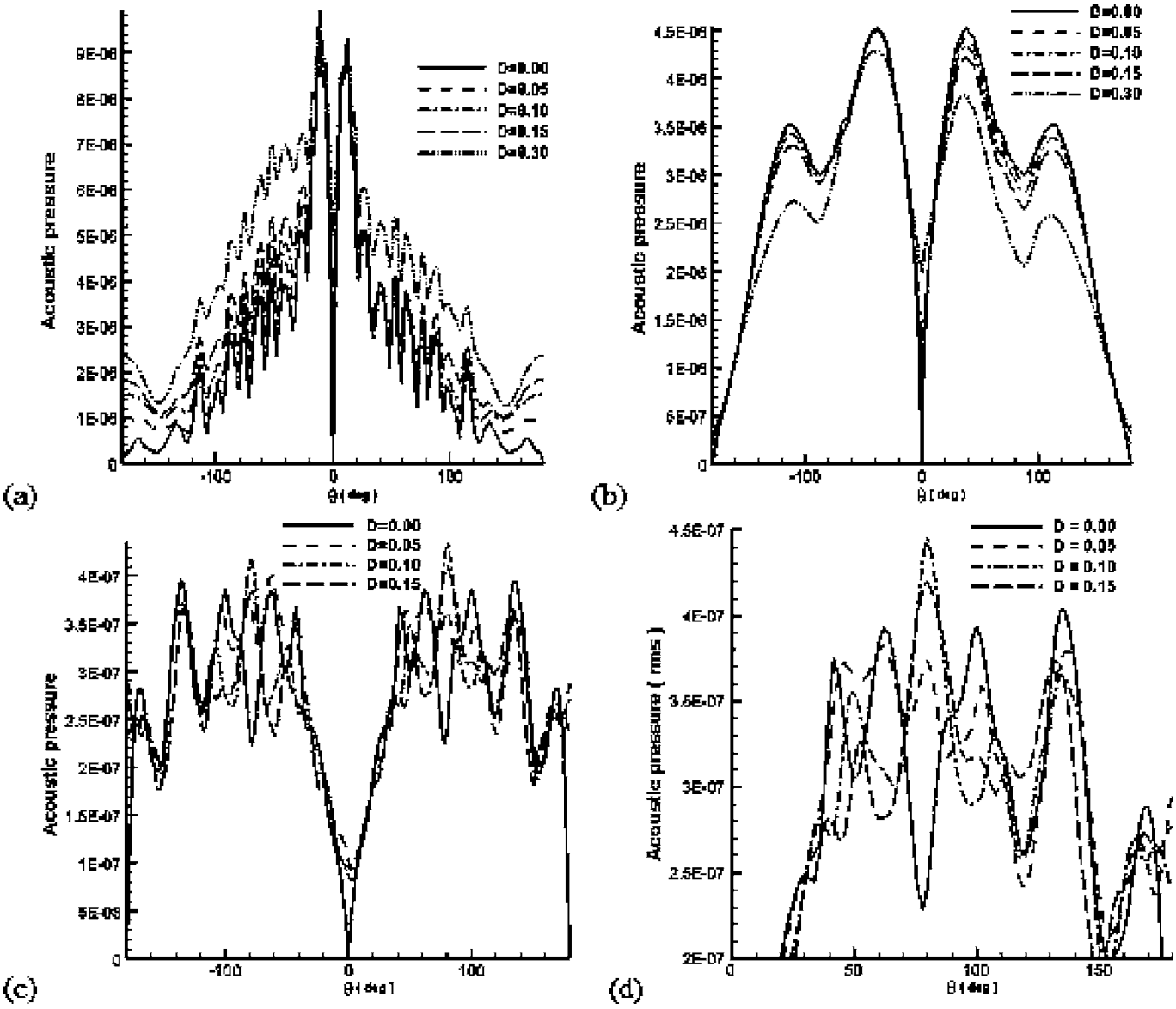

FIG. 8. The RMS of acoustic pressure radiated by the two-row vortex street with the range of proximity between rows: (a) frequency $f=1/0.05$, (b,c) frequency $f=1/0.5$; (a,b) Vatistas' vortex street, (c,d) Taylor's vortex street. Here (d) is an enlargement of (c) to show fluctuations of acoustic pressure with D.

(this was also observed by Gursul and Rockwell[1]). For the low-frequency case, the vortices keep their identity; the extent of vortex distortion is determined by the vortex location in the mean flow. For the high-frequency case, the vortices are merged. Observing the initial distribution of vorticity for Taylor's vortex [Fig. 1(b)] and the distribution of vorticity while Taylor vortices are convected about the cylinder [Fig. 9(b)] shows that the vorticity has positive and negative parts; that is not the case for chains of Vatistas' vortices [Fig. 9(a)]. The opposite-sign vorticity forms continuous bands for high-frequency Taylor vortices and concentric peripheral areas around individual vortices for low-frequency chains. On the one hand, the maximum of vorticity is 50% larger for the Taylor vortex than that for the Vatistas vortex when vortices are added to the flow [see Fig. 1(b)]. On the other hand, the maximum level of vorticity is moderately larger for Vatistas' vortex chain [compare the legend in Figs 9(a) and 9(b)]. This is caused by the interference of tails of neighboring vortices.

In the following parametric investigation of sound directivity of vortex streets impinging on the cylinder, the vortex street with spacing $D=0.1$ was taken as the representative case. In Fig. 10, the RMS of P_{acous} is presented with respect to angle θ at different vortex street frequencies. Qualitatively, the results are similar to those obtained for $D=0$ (see Fig. 6). For higher frequency, more vortices are embedded in the mean flow and impinge on the cylinder surface per time unit. Thus, for both the Vatistas and the Taylor vortex streets, the sound pressure amplitude is observed to increase with frequency.

For a low-frequency Vatistas vortex street, a distinct maximum sound directivity was observed. However, the sound directivity is different for each frequency and changes from 30° to 40° when the frequency varies from 1/1.00 to 1/0.05 [Fig. 10(a)]. For the high-frequency Vatistas vortex

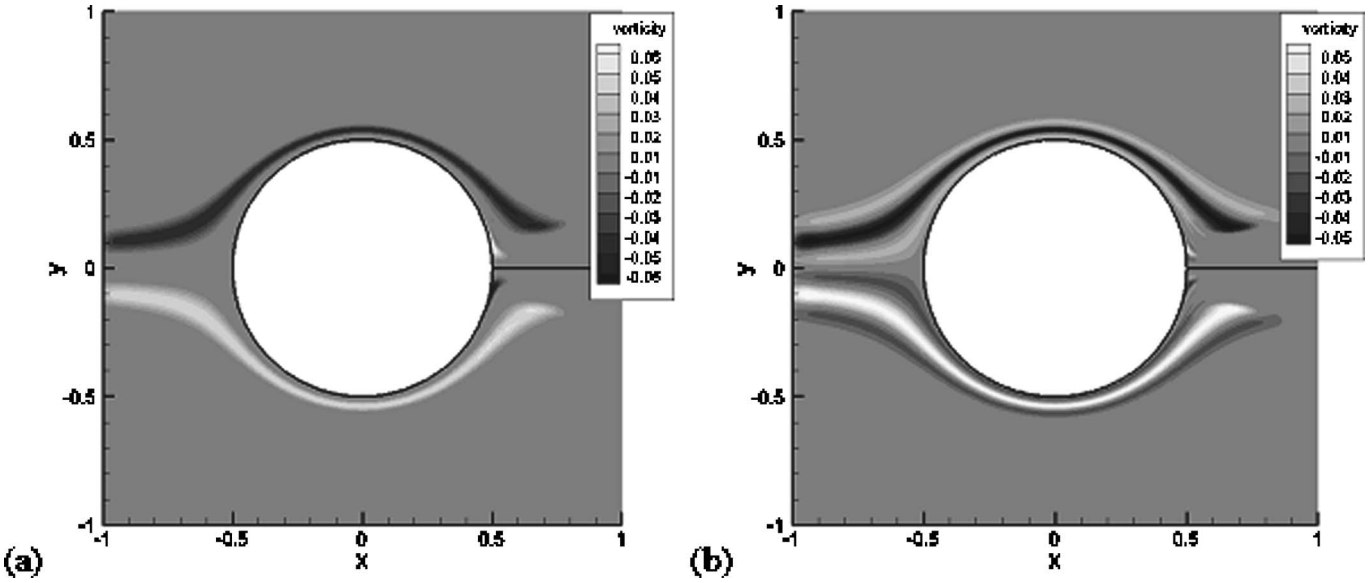

FIG. 9. Vorticity distribution for a two-row vortex street at $f=20$: (a) Vatistas' vortex street and (b) Taylor's vortex street.

street, the amplitude change with the frequency is quite moderate. As the frequency rises, the sound profile becomes more nonmonotonic. For the vortex street at high frequency, there is a well-defined maximum sound directivity at $\sim 10°$ with the centerline. The presence of silence zone is observed for the low-frequency Taylor vortex street. In comparison to Vatistas' vortex street, the sound pressure amplitude is almost ten times smaller for the same vortex core size and vortex strength. A prominent sound level in the downstream centerline is observed for the Taylor vortex street.

Next, the effect of the mean flow Mach number was investigated. It was observed that as the mean flow Mach number increases, the vortices become more deformed and appear closer to the cylinder's surface. In turn, the RMS of acoustic pressure will significantly increase in amplitude (see Fig. 11). For the low-frequency Vatistas vortex street, as the Mach number of mean flow increases, the sound directivity is slightly shifted toward the centerline. In particular, the sound directivity shifts from 10° for $M_\infty=0.1$ to 70° for $M_\infty=0.4$ [Fig. 11(b)]. In the case of the high-frequency Vatistas vortex street, the mean flow Mach number has a moderate effect on the sound wave profile as compared to the low-frequency vortex street [compare Figs. 11(a) and 11(b)]. The mean flow Mach number affects greatly the sound pressure level when a low-frequency Taylor vortex street is considered. Furthermore, the sound directivity is shifted from the centerline and corresponds to 60° for $M_\infty=0.4$ [see Fig. 11(c)].

Since low-amplitude vortices are examined using linearized Euler equations, the strength of the RMS of acoustic pressure appears to be proportional to the vortex strength (circulation) for both the Vatistas vortex street and the Taylor vortex street. That is, the RMS of acoustic pressure can be

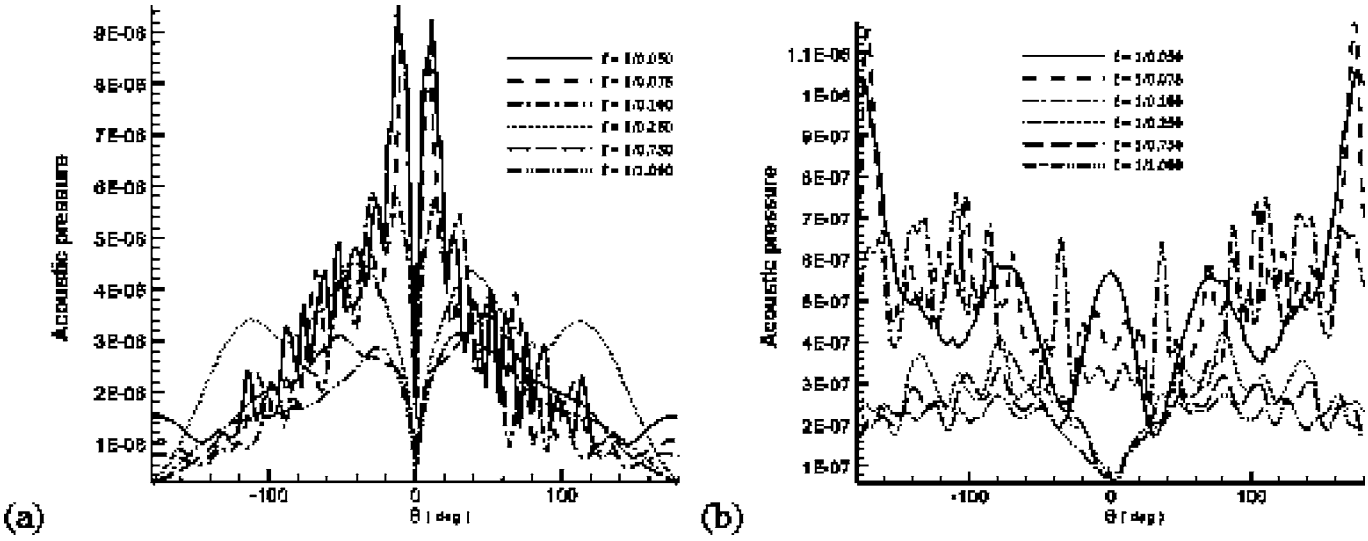

FIG. 10. The RMS of acoustic pressure for a different vortex adding frequency: (a) Vatistas' vortex street and (b) Taylor's vortex street.

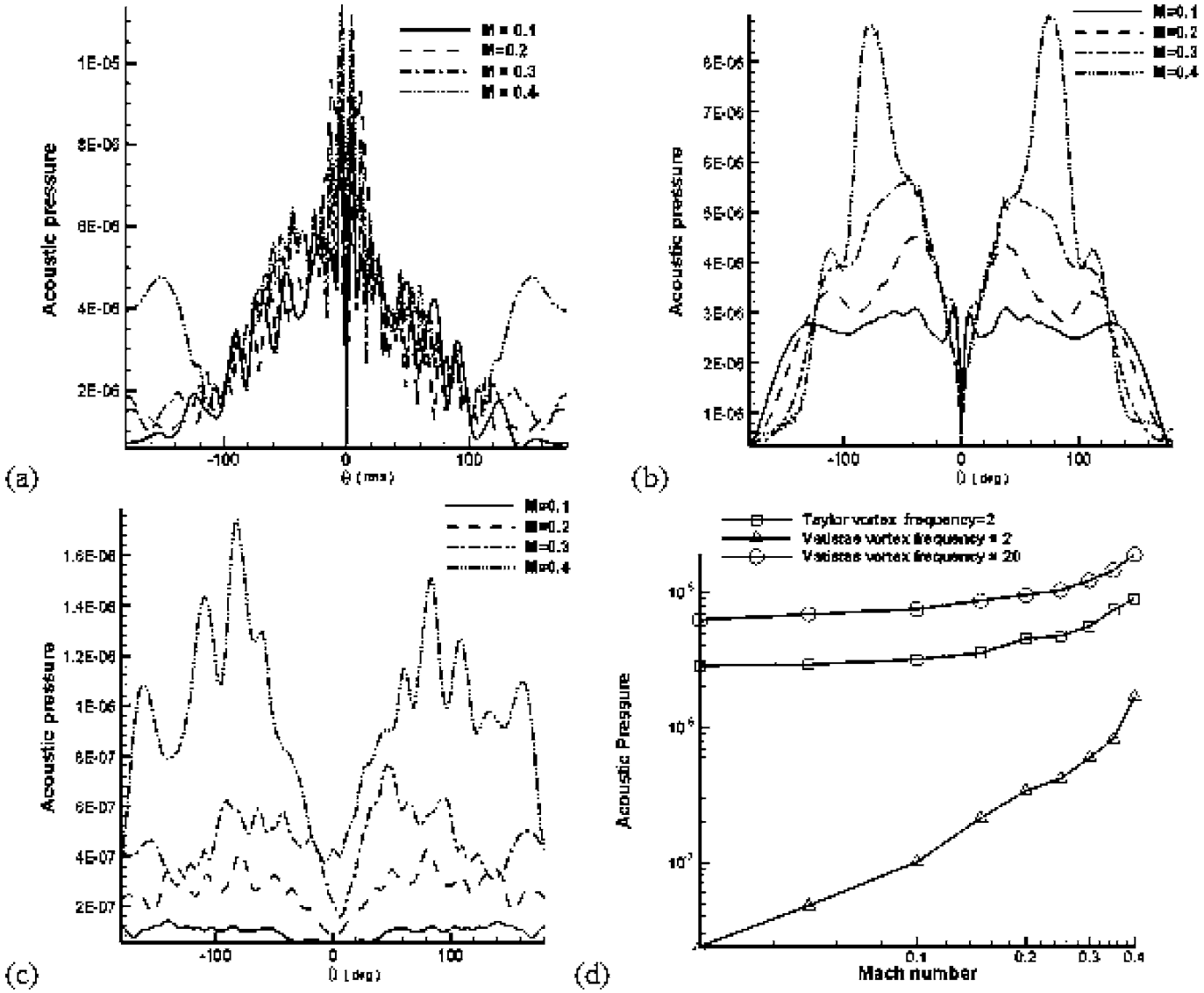

FIG. 11. The RMS of acoustic pressure for various Mach numbers of the mean flow: (a) Vatistas' vortex street at frequency $f=20$, (b) Vatistas' vortex street at frequency $f=2$, (c) Taylor's vortex street at frequency $f=2.0$.

normalized by the vortex strength, and the normalized RMS curves coincide.

The studies by Kambe, Minota, and Takaoka[27] and Kamble[28] show that the amplitude of acoustic pressure of compact vortex-cylinder interaction is $O(M^3)$, where M is the Mach number of the flow in infinity. The magnitude of acoustic pressure for Taylor and Vatistas vortices as functions of the Mach number in log-log coordinates is shown in Fig. 11(d). The average value of the power p in $O(M^p)$ is 0.41 for Vatistas' vortices and 1.57 for Taylor's vortices. The value of p is practically the same for low-frequency and high-frequency Vatistas vortex chains. The value of $p=3$ was obtained under the assumption of compact vortices; therefore, the value of p for the Vatistas vortices with the distributed velocity profile does not match $p=3$. The value of p for more localized Taylor vortices is larger and, therefore, closer to the analytical evaluation of p.

The effect of the vortex core size on the sound generation and propagation was investigated and shown in Fig. 12. The RMS of acoustic pressure corresponding to the high-frequency and low-frequency vortex street was presented using vortices of different core sizes for the Vatistas vortex street and the Taylor vortex street, respectively. Each vortex was kept at the same vortex strength with the circulation equal to 0.00005, whereas core radius was set at 0.04, 0.10, and 0.20, respectively. It is observed that the variation of the vortex core size had quite a different effect on Vatistas and Taylor vortices. For the Vatistas vortex street, the amplitude of RMS acoustic pressure increases slightly with an increase of the core size, albeit the sound directivity remains unchanged. Overall, the variation of the vortex core size has a very modest effect on the noise generated by both low-frequency and high-frequency chains of Vatistas' vortices [see Figs. 12(a) and 12(b)]. On the contrary, for the Taylor vortex street the variation of vortex core size not only changed the sound amplitude significantly, but also changed the angular profile of acoustic pressure [Fig. 12(c)]. The sound directivity is shifted closer to the centerline with an

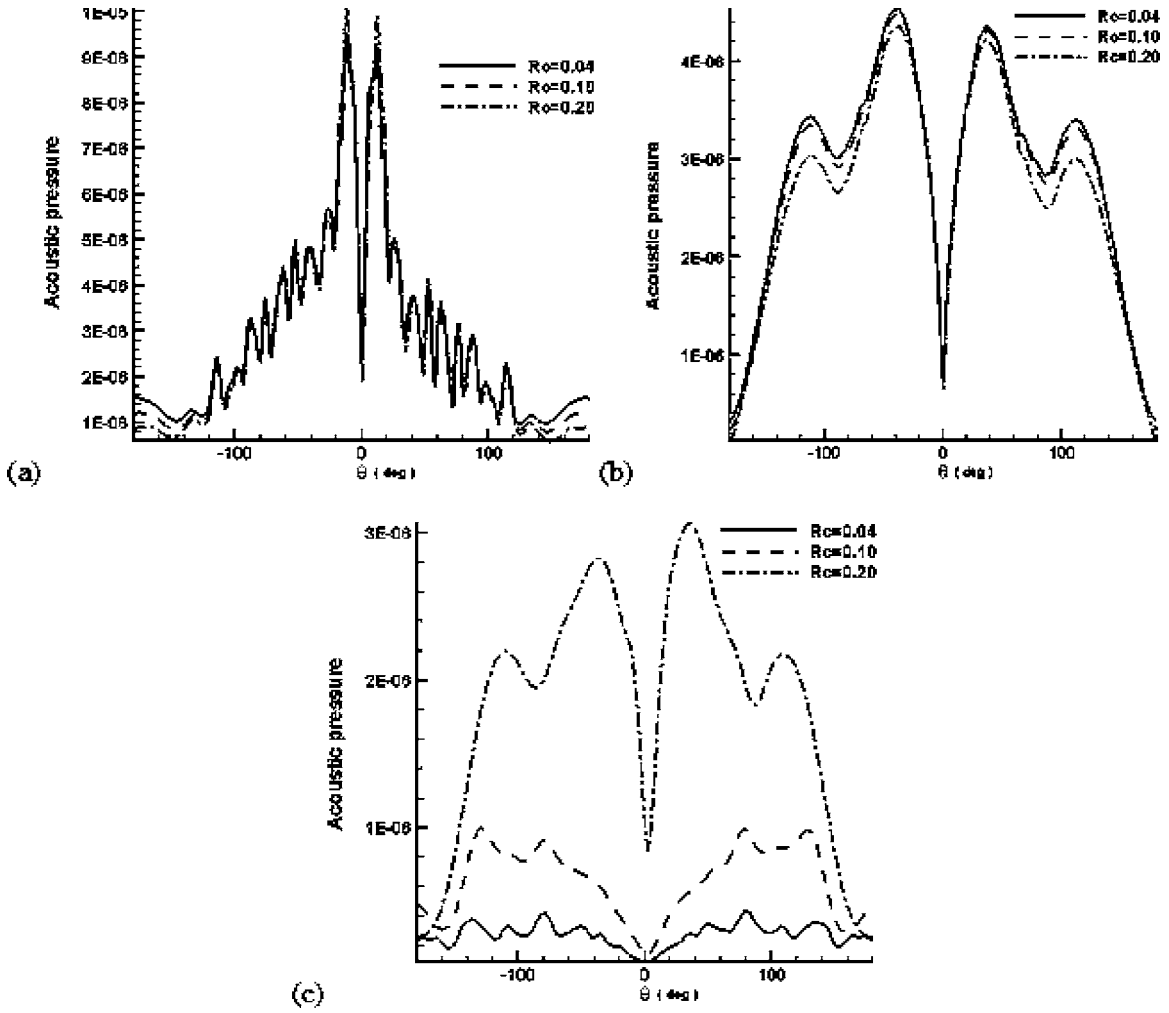

FIG. 12. The RMS of acoustic pressure for various sizes of the vortex core: Vatistas' vortex street (a,b), Taylor's vortex street (c), where $f=20$ (a,c) and $f=2$ (b).

increase of the vortex core size. In summary, while maintaining a constant circulation, a moderate core increase of Taylor's vortex greatly amplifies the sound level.

V. CONCLUSIONS

The objective of the study is to provide computational insight into the propagation of acoustic waves generated by chains of noncompact vortices impinging on a rigid body immersed in a nonuniform subsonic flow. The propagation of acoustic waves that originate from self-similar periodic vortices is studied numerically using a high-order compact finite-difference approximation of the linearized Euler equations in terms of unsteady disturbances. The goal of the study is to develop a simple mean flow model through the expansion around a steady subsonic compressible flow about a cylinder, where the coefficients in the linearized system are replaced by an incompressible approximation. The vortex ensembles, categorized as low- and high-frequency vortex streets, determine the degree of interaction among them. It was discovered that the vortex-body interaction mechanism, sound generation, and propagation in a nonuniform flow are quite different for Taylor's and Vatistas' vortex streets.

For the low-frequency Vatistas vortex street, the RMS of acoustic pressure has a monotonic sound directivity. The sound amplitude and its directivity are greatly affected by the Mach number of the mean flow (see Fig. 11). For the high-frequency Vatistas vortex street, the RMS of acoustic pressure became highly nonmonotonic, whereas the Mach number of the mean flow has a very moderate effect on the RMS acoustic pressure profile. For the low-frequency Taylor vortex street, the RMS of acoustic pressure is monotonic, and the Mach number of the mean flow significantly affects its sound amplitude and directivity. The average value of the power p in $O(M^p)$ is equal to 0.41 for Vatistas' vortices and 1.57 for Taylor's vortices. The p value is practically the same for the low-frequency and the high-frequency Vatistas vortex chains. The value of $p=3$ was obtained under the assumption of compact vortices, therefore the p value for Vatistas' vortices with the distributed velocity profile does not match $p=3$. The p value for more local Taylor vortices is larger and, therefore, closer to the analytical evaluation of p.

The vortex core size and vortex street spacing are found to have a minor effect on the acoustic pressure amplitude for the Vatistas vortex street. Nevertheless, the vortex core size and the spacing between vortex rows significantly affect the

character of the sound wave radiated by the Taylor vortex street (see Figs. 8 and 12).

The distribution of vorticity in vortices is analyzed from the vortex addition to the mean flow to its impingement on the cylinder and convection about the cylinder surface. Taylor's vortex has positive and negative vorticity parts that are retained throughout the impingement and convection of vortices. In spite of the higher initial level of maximum vorticity for Taylor's vortex as compared to that of Vatistas, the level of RMS acoustic pressure is orders of magnitude larger for the impinging Vatistas vortices than that for Taylor's. The sound that originates from the impingement of Taylor's vortices is highly nonmonotonic with respect to the centerline. The reduced RMS for Taylor's vortices and the highly nonmonotonic directivity of RMS (see Fig. 6) can be explained by the interference and mutual cancellation of the positive and negative parts of vorticity in the integral for the acoustic pressure. The magnitude of the latter property is proportional to $\int \vec{\omega} * \vec{v}$. For Vatistas' model, the sign of vorticity remains the same, whereas for Taylor's vortex the sign alternates. The area of nonzero vorticity remains approximately the same for both vortices [see Fig. 1(b)]. Therefore, the mutual cancellations of the opposite-sign contributions in the previously mentioned integral lead to a smaller acoustic pressure for Taylor's vortex.

APPENDIX A: THE LINEARIZED DYNAMIC EQUATIONS FOR DISTURBANCE COMPONENTS

The nonlinear Euler equations for the unsteady disturbance components in Cartesian coordinates yield

$$(R+\rho')\frac{\partial(U+u')}{\partial t} = -\frac{\partial(P+p')}{\partial x} - (U+u')(R + \rho')\frac{\partial(U+u')}{\partial x} - (V+v')(R + \rho')\frac{\partial(U+u')}{\partial y},$$

$$(R+\rho')\frac{\partial(V+v')}{\partial t} = -\frac{\partial(P+p')}{\partial y} - (U+u')(R + \rho')\frac{\partial(V+v')}{\partial y} - (V+v')(R + \rho')\frac{\partial(V+v')}{\partial y},$$

$$\frac{\partial(R+\rho')}{\partial t} = -\frac{\partial(U+u')(R+\rho')}{\partial x} - \frac{\partial(V+v')(R+\rho')}{\partial y},$$

$$p' = c^2\rho', \tag{A1}$$

where R is the mean flow density. The variables in (A1) have been nondimensionalized by the following scales:

Length scale=characteristic length, $L=D$, where D is the diameter of the cylinder.

Velocity scale=the ambient speed of sound, c_∞.

Time scale=L/c_∞.

Density scale=the ambient gas density, ρ_∞.

Pressure scale=$\rho_\infty c_\infty^2$.

Neglecting the products of disturbance variables and subtracting the mean flow equations, the linearized Euler equations with respect to disturbances are obtained,

$$\frac{\partial\rho'}{\partial t} = -R\left(\frac{\partial u'}{\partial x} + \frac{\partial v'}{\partial y}\right) - U\frac{\partial\rho'}{\partial x} - V\frac{\partial\rho'}{\partial y} - u'\frac{\partial R}{\partial x} - v'\frac{\partial R}{\partial y} - \rho'\left(\frac{\partial U}{\partial x} + \frac{\partial V}{\partial y}\right),$$

$$\frac{\partial u'}{\partial t} = -\frac{1}{R}\frac{\partial p'}{\partial x} - U\frac{\partial v'}{\partial y} - V\frac{\partial u'}{\partial y} - \frac{\partial U}{\partial x}u' - \frac{\partial U}{\partial y}v' - \left(U\frac{\partial U}{\partial x} + V\frac{\partial U}{\partial y}\right)\frac{\rho'}{R},$$

$$\frac{\partial v'}{\partial t} = -\frac{1}{R}\frac{\partial p'}{\partial y} - V\frac{\partial v'}{\partial y} - U\frac{\partial v'}{\partial x} - \frac{\partial V}{\partial x}u' - \frac{\partial V}{\partial y}v' - \left(U\frac{\partial V}{\partial x} + V\frac{\partial V}{\partial y}\right)\frac{\rho'}{R},$$

$$p' = c^2\rho'. \tag{A2}$$

Equations (A2) are simplified so that the mean flow is replaced with its incompressible approximation. As shown below, the error of this approximation is of the order of $O(M_\infty^2)$. First, the error introduced by the replacement of the compressible velocity field with its incompressible approximation is investigated. The compressible velocity potential is given by

$$\phi = U_\infty(\phi_0 + M_\infty^2\phi_1) + O(M_\infty^4), \tag{A3}$$

where ϕ_0 is the incompressible velocity potential, and $M_\infty^2\phi_1$ is $O(M_\infty^2)$ correction to the incompressible velocity potential given by Janzen and Rayleigh and cited in Ref. 29. The ϕ_0 and ϕ_1 are independent on the Mach number. The analytical expressions for ϕ_0 and ϕ_1 are given in Ref. 29, p. 12. The velocity components are split accordingly to incompressible and compressible parts, which are gradients of ϕ_0 and ϕ_1,

$$U = U_0 + U_1, V = V_0 + V_1. \tag{A4}$$

To split (A2) to compressible and incompressible components, the above sums (A4) are substituted to (A2) to yield

$$\frac{\partial\rho'}{\partial t} = -R\left(\frac{\partial u'}{\partial x} + \frac{\partial v'}{\partial y}\right) - U_0\frac{\partial\rho'}{\partial x} - V_0\frac{\partial\rho'}{\partial y} - u'\frac{\partial R}{\partial x} - v'\frac{\partial R}{\partial y} - \rho'\left(\frac{\partial U_0}{\partial x} + \frac{\partial V_0}{\partial y}\right) - U_1\frac{\partial\rho'}{\partial x} - V_1\frac{\partial\rho'}{\partial y} - \rho'\left(\frac{\partial U_1}{\partial x} + \frac{\partial V_1}{\partial y}\right),$$

$$\frac{\partial u'}{\partial t} = -\frac{1}{R}\frac{\partial p'}{\partial x} - U_0\frac{\partial v'}{\partial y} - V_0\frac{\partial u'}{\partial y} - \frac{\partial U_0}{\partial x}u' - \frac{\partial U_0}{\partial y}v' - \left(U_0\frac{\partial U_0}{\partial x} + V_0\frac{\partial U_0}{\partial y}\right)\frac{\rho'}{R} - U_1\frac{\partial v'}{\partial y} - V_1\frac{\partial u'}{\partial y} - \frac{\partial U_1}{\partial x}u' - \frac{\partial U_1}{\partial y}v' - \left(U_1\frac{\partial U_0}{\partial x} + V_1\frac{\partial U_0}{\partial y} + (U_0 + U_1)\frac{\partial U_1}{\partial x} + (V_0 + V_1)\frac{\partial U_1}{\partial y}\right)\frac{\rho'}{R},$$

$$\frac{\partial v'}{\partial t} = -\frac{1}{R}\frac{\partial p'}{\partial y} - V_0\frac{\partial v'}{\partial y} - U_0\frac{\partial v'}{\partial x} - \frac{\partial V_0}{\partial x}u' - \frac{\partial V_0}{\partial y}v' - \left(U_0\frac{\partial V_0}{\partial x} + V_0\frac{\partial V}{\partial y}\right)\frac{\rho'}{R} - V_1\frac{\partial v'}{\partial y} - U_1\frac{\partial v'}{\partial x} - \frac{\partial V_1}{\partial x}u' - \frac{\partial V_1}{\partial y}v' - \left(\frac{\partial V_0}{\partial x} + V_1\frac{\partial V}{\partial y} + (U_0 + U_1)\frac{\partial V_1}{\partial x} + (V_0 + V_1)\frac{\partial V_1}{\partial y}\right)\frac{\rho'}{R},$$

$$p' = c^2\rho'. \tag{A5}$$

The set (A6) is obtained as follows:

$$\frac{\partial \rho'}{\partial t} = -R\left(\frac{\partial u'}{\partial x} + \frac{\partial v'}{\partial y}\right) - U_0\frac{\partial \rho'}{\partial x} - V_0\frac{\partial \rho'}{\partial y} - u'\frac{\partial R}{\partial x} - v'\frac{\partial R}{\partial y} - \rho'\left(\frac{\partial U_0}{\partial x} + \frac{\partial V_0}{\partial y}\right) + \text{H.O.T.},$$

$$\frac{\partial u'}{\partial t} = -\frac{1}{R}\frac{\partial p\,'}{\partial x} - U_0\frac{\partial v'}{\partial y} - V_0\frac{\partial u'}{\partial y} - \frac{\partial U_0}{\partial x}u' - \frac{\partial U_0}{\partial y}v' - \left(U_0\frac{\partial U_0}{\partial x} + V_0\frac{\partial U_0}{\partial y}\right)\frac{\rho'}{R} + \text{H.O.T.},$$

$$\frac{\partial v'}{\partial t} = -\frac{1}{R}\frac{\partial p\,'}{\partial y} - V_0\frac{\partial v'}{\partial y} - U_0\frac{\partial v'}{\partial x} - \frac{\partial V_0}{\partial x}u' - \frac{\partial V_0}{\partial y}v' - \left(U_0\frac{\partial V_0}{\partial x} + V_0\frac{\partial V}{\partial y}\right)\frac{\rho'}{R} + \text{H.O.T.},$$

$$p' = c^2\rho', \tag{A6}$$

where H.O.T.$=O(M_\infty^2)+O(M_\infty^4)$ are high-order terms.

The high-order terms correspond to U_1 and V_1 components of mean flow in Eqs. (A5). In particular, the $O(M_\infty^2)$ terms contain U_1 and V_1, whereas the terms containing products $U_1 \times V_1$ are of $O(M_\infty^4)$.

Next, the estimate of error, introduced by using uniform density and speed of sound, is obtained. The isentropic relation for perfect gas flow[30] between states *0* and *1* yields

$$\frac{\rho_0}{\rho_1} = \left(\frac{1 + 0.5(\gamma-1)M_1^2}{1 + 0.5(\gamma-1)M_0^2}\right)^{1/(\gamma-1)}. \tag{A7}$$

By multiplying the nominator and the denominator by $1 - 0.5(\gamma-1)M_0^2$ and neglecting $O(M^4)$, the local density R and the local speed of sound are given by

$$R = \left[1 - \frac{\gamma-1}{2}(M^2 - M_\infty^2)\right]^{1/(\gamma-1)},$$

$$c = \left[1 - \frac{\gamma-1}{2}(M^2 - M_\infty^2)\right]^{1/2}. \tag{A8}$$

Here M is the local Mach number, $M^2 = U^2 + V^2$. Recall that density and the speed of sound are equal to unity in the far field where the normalized mean flow speed is equal to M_∞. Taking Taylor expansion of the first equation with respect to $z = M^2 - M_\infty^2$ about $z=0$, the following approximate relations are obtained:

$$R = 1 - 0.5(M^2 - M_\infty^2) + O(M_\infty^4),$$

$$c^2 = 1 - 0.5(\gamma-1)(M^2 - M_\infty^2),$$

$$1/R = 1 + 0.5(M^2 - M_\infty^2) + O(M_\infty^4). \tag{A9}$$

Similar relations for the density of mean flow and the speed of sound are used in aeroacoustic compressible computations.[31] Equations (A9) are substituted into (A6) to yield

$$\frac{\partial \rho'}{\partial t} = -[1 - 0.5(M^2 - M_\infty^2)]\left(\frac{\partial u'}{\partial x} + \frac{\partial v'}{\partial y}\right) - U_0\frac{\partial \rho'}{\partial x} - V_0\frac{\partial \rho'}{\partial y} - \rho'\left(\frac{\partial U_0}{\partial x} + \frac{\partial V_0}{\partial y}\right) - u'\frac{\partial[1 - 0.5(M^2 - M_\infty^2)]}{\partial x} - v'\frac{\partial[1 - 0.5(M^2 - M_\infty^2)]}{\partial y} + \text{H.O.T.},$$

$$\frac{\partial u'}{\partial t} = -[1 + 0.5(M^2 - M_\infty^2)]\frac{\partial p'}{\partial x} - U_0\frac{\partial v'}{\partial y} - V_0\frac{\partial u'}{\partial y} - \frac{\partial U_0}{\partial x}u' - \frac{\partial U_0}{\partial y}v' - \left(U_0\frac{\partial U_0}{\partial x} + V_0\frac{\partial U_0}{\partial y}\right)[1 + 0.5(M^2 - M_\infty^2)]\rho' + \text{H.O.T.},$$

$$\frac{\partial v'}{\partial t} - [1 + 0.5(M^2 - M_\infty^2)]\frac{\partial p'}{\partial y} - V_0\frac{\partial v'}{\partial y} - U_0\frac{\partial v'}{\partial x} - \frac{\partial V_0}{\partial x}u' - \frac{\partial V_0}{\partial y}v' - \left(U_0\frac{\partial V_0}{\partial x} + V_0\frac{\partial V}{\partial y}\right)[1 + 0.5(M^2 - M_\infty^2)]\rho' + \text{H.O.T.},$$

$$p' = [1 - 0.5(\gamma-1)(M^2 - M_\infty)]\rho' + \text{H.O.T.}, \tag{A10}$$

where H.O.T.$=O(M_\infty^2)+O(M_\infty^4)+O(M_\infty^6)$ are obtained by substitution of (A9) to the H.O.T. in (A6). The $O(M_\infty^2)$ and $O(M_\infty^4)$ H.O.T. terms in (A6), being multiplied by $M^2 - M_\infty^2$, become $O(M_\infty^4)$ and $O(M_\infty^6)$, in correspondence.

Omitting the components having multipliers $M^2 - M_\infty^2$, $\partial(M^2)/\partial x$, and $\partial(M^2)/\partial y$ in the above equations, the incompressible approximate model is obtained,

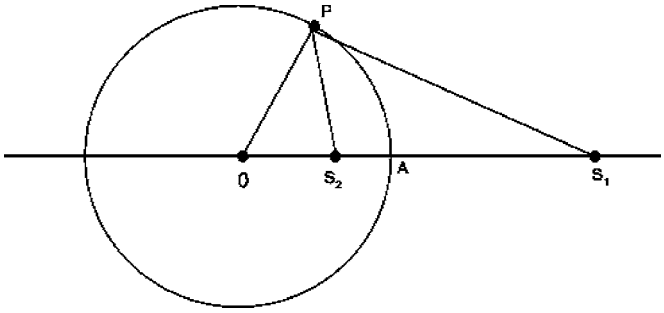

FIG. 13. Image of a vortex in a fixed circular cylinder.

$$\frac{\partial p'}{\partial t} = -\left(\frac{\partial u'}{\partial x} + \frac{\partial v'}{\partial y}\right) - U_0\frac{\partial p'}{\partial x} - V_0\frac{\partial p'}{\partial y} - p'\left(\frac{\partial U_0}{\partial x} + \frac{\partial V_0}{\partial y}\right),$$

$$\frac{\partial u'}{\partial t} = -\frac{\partial p'}{\partial x} - U_0\frac{\partial v'}{\partial y} - V_0\frac{\partial u'}{\partial y} - \frac{\partial U_0}{\partial x}u' - \frac{\partial U_0}{\partial y}v' - \left(U_0\frac{\partial U_0}{\partial x} + V_0\frac{\partial U_0}{\partial y}\right)p',$$

$$\frac{\partial v'}{\partial t} = -\frac{\partial p'}{\partial y} - V_0\frac{\partial v'}{\partial y} - U_0\frac{\partial v'}{\partial x} - \frac{\partial V_0}{\partial x}u' - \frac{\partial V_0}{\partial y}v' - \left(U_0\frac{\partial V_0}{\partial x} + V_0\frac{\partial V}{\partial y}\right)p'. \quad \text{(A11)}$$

APPENDIX B: THE VORTEX IMAGE SYSTEM SETUP

When the vortex flow field with circulation Γ is implemented as an initial condition at S_1, it might violate the nonpenetrating boundary condition if its core reaches the rigid wall. On the cylinder wall, to satisfy the zero normal velocity boundary condition, a vortex image system is employed at time steps when the vortices were added and switched off otherwise.

The two image vortices are added at points S_2 and O. The inverse points S_1 and S_2 lie on a line OA through the center O of the circle (see Fig. 13) and satisfy $OS_1 \cdot OS_2 = OA^2$. Triangle OPS_1 and triangle OPS_2 are similar. Because of this property, the following ratio holds:

$$S_2P:S_1P = OP:OS_1 = \text{const}. \quad \text{(B1)}$$

The image vortex system consists of an equal but oppositely spinning vortex with circulation-Γ at the inverse point S_2, and an equal vortex with the same circulation Γ at the origin O.[23]

For this system of vortices, the cylinder surface is a streamline, therefore a rigid boundary can be placed there without altering the flow. The image vortices located at O and S_2 give zero circulation at infinity, that is, the circulation of the system of three vortices is equal to the original circulation Γ of the vortex located at S_1.

At each time step t when the vortex is added, the velocity field created by the vortex image system is added to the old values u', v' obtained by the numerical solution of the system of PDEs (2),

$$u'_{\text{new}}(t) = u'_{\text{old}}(t) + u_{\text{vor}},$$

$$v'_{\text{new}}(t) = v'_{\text{old}}(t) + v_{\text{vor}}, \quad \text{(B2)}$$

where u_{vor}, v_{vor} are the velocity components created by the image vortex system.

[1] I. Gursul and D. Rockwell, "Vortex street impinging upon an illiptical leading edge," J. Fluid Mech. **211**, 211 (1990).
[2] M. M. Choudhary and M. R. Khorrami, "Slat cove unsteadiness: Effect of 3-D flow structures," AIAA Paper 2006-0211, presented at the 44th AIAA Aerospace Science Meeting and Exhibit, Reno, NV (2006).
[3] N. Curle, "The influence of solid boundaries upon aerodynamic sound," Proc. R. Soc. London, Ser. A **231**, 505 (1955).
[4] G. Lilley, "The prediction of airframe noise," J. Sound Vib. **239**, 849 (2001).
[5] S. S. Collis, K. Ghayour, and M. Heinkenschloss, "Optimal control of aeroacoustic noise generated by cylinder vortex interaction," International Journal of Aeroacoustics **1**, 97 (2002).
[6] D. Rockwell, "Vortex-body interactions," Annu. Rev. Fluid Mech. **30**, 199 (1998).
[7] S. E. Widnall, "Helicopter noise due to blade/vortex interaction," J. Acoust. Soc. Am. **50**, Pt. 2, 354 (1971).
[8] A. Povitsky, "Numerical study of wave propagation in a nonuniform compressible flow," Phys. Fluids **14**, 2657 (2002).
[9] M. J. Lighthill, "On sound generated aerodynamically: I. General theory," Proc. R. Soc. London, Ser. A **211**, 564 (1952).
[10] O. Inoue and Y. Hattori, "Sound generation by shock-vortex interactions," J. Fluid Mech. **380**, 81 (1999).
[11] M. J. Bhagwat and J. G. Leishman, "Generalized viscous vortex model for application to free-vortex wake and aeroacoustics," *Proceedings of the 58th Annual Forum of the American Helicopter Society*, June, Montreal, Canada (American Helicopter Society, 2002), ISSN: 1552-2938.
[12] G. H. Vatistas, "New model for intense self-similar vortices," J. Propul. Power **14**, 462 (1998).
[13] T. Colonius, S. K. Lele, and P. Moin, "The scattering of sound waves by a vortex: Numerical simulations and analytical solutions," J. Fluid Mech. **260**, 271 (1994).
[14] M. R. Visbal and D. V. Gaitonde, "High-order accurate methods for complex unsteady subsonic flows," AIAA J. **37**, 1231 (1999).
[15] A. Povitsky, T. Zheng, and G. Vatistas, "Effect of vortex profile on sound generation in a non-uniform flow," Math. Comput. Simul. **65**, 447 (2004).
[16] T. Zheng, G. Vatistas, and A. Povitsky, "Sound generation by one-cell and two-cell vortices," J. Comput. Acoust. **14**, 321 (2006).
[17] J. Hardin and D. S. Pope, "A new technique for aerodynamic noise calculation," *Proceedings of the DGLRR/AIAA 14th Aeroacoustics Conference*, Washington, DC (1992), pp.448–456.
[18] S. A. Slimon, M. Soteriou, and D. Davis, "Computational aeroacoustics simulations using the expansion about incompressible flow approach," AIAA J. **37**, 409 (1999).
[19] B. A. Singer, K. S. Brentner, D. P. Lockard, and G. M. Lilley, "Simulation of acoustic scattering from a trailing edge, J. Sound Vib. **230** 541 (2000).
[20] S. K. Lele, "Compact finite difference scheme with spectral like resolution," J. Comput. Phys. **103**, 16 (1992).
[21] J. Williamson, "Low-storage Runge-Kutta schemes," J. Comput. Phys. **35**, 48 (1980).
[22] G. I. Taylor, "On the dissipation of eddies," *The Scientific Papers of Sir Geoffrey Ingram Taylor* (Cambridge University Press, Cambridge, UK, 1958), Vol. 2, pp. 96–101.
[23] W. J. Duncan, A. S. Thom, and A. D. Young, *Mechanics of Fluids* (Edward Arnold LTD, London, 1970).
[24] F. Q. Hu, "A stable, perfectly matched layer for linearized Euler equations in unsplit physical variables," J. Comput. Phys. **173**, 455 (2001).
[25] A. Povitsky, T. Zheng, and G. Vatistas, "Numerical study on propagation and scattering of sound by two cylinders," *Proceedings of the 4th CAA Workshop on Benchmark Problems* (Ohio Aerospace Institute, Cleveland, 2003), pp. 283–290.

[26]M. S. Howe, *Theory of Vortex Sound* (Cambridge University Press, Cambridge, UK, 2002).
[27]T. Kambe, T. Minota, and M. Takaoka, "Oblique collision of two vortex rings and its acoustic emission," Phys. Rev. E **48**, 1866 (1993).
[28]T. Camble, "Acoustic emissions by vortex motions," J. Fluid Mech. **173**, 643 (1986).
[29]J. Lighthill, *Higher Approximation in Aerodynamic Theory* (Princeton University Press, Princeton, NJ, 1960).
[30]M. A. Saad, *Compressible Fluid Flow*, 2nd ed. (Prentice Hall, Englewood Cliffs, NJ, 1993).
[31]W. Eversman and D. Okunbor, "Aft fan duct acoustic radiation," J. Sound Vib. **213**, 235 (1998).